


Dense, high-resolution mapping of cells and tissues from pathology images for the interpretable prediction of molecular phenotypes in cancer

*James A. Diao^{1,2}, *Wan Fung Chui^{1,2}, *Jason K. Wang^{1,2}, Richard N. Mitchell^{2,3}, Sudha K. Rao¹, Murray B. Resnick^{1,4}, Abhik Lahiri¹, Chirag Maheshwari¹, Benjamin Glass¹, Victoria Mountain¹, Jennifer K. Kerner¹, Michael C. Montalto¹, Aditya Khosla¹, Ilan N. Wapinski¹, *Andrew H. Beck¹, , *Amaro Taylor-Weiner¹, and *Hunter L. Elliott¹

¹PathAI, Inc., Boston, MA, 02215, USA

²Harvard-MIT Program in Health Sciences and Technology, Harvard Medical School, Boston, MA, 02115, USA

³Department of Pathology, Brigham and Women's Hospital, Harvard Medical School, Boston, Massachusetts

⁴Department of Pathology, Warren Alpert Medical School of Brown University, Providence, Rhode Island

[†]These authors contributed equally

While computational methods have made substantial progress in improving the accuracy and throughput of pathology workflows for diagnostic, prognostic, and genomic prediction, lack of interpretability remains a significant barrier to clinical integration. In this study, we present a novel approach for predicting clinically-relevant molecular phenotypes from histopathology whole-slide images (WSIs) using human-interpretable image features (HIFs). Our method leverages >1.6 million annotations from board-certified pathologists across >5,700 WSIs to train deep learning models for high-resolution tissue classification and cell detection across entire WSIs in five cancer types. Combining cell- and tissue-type models enables computation of 607 HIFs that comprehensively capture specific and biologically-relevant characteristics of multiple tumors. We demonstrate that these HIFs correlate with well-known markers of the tumor microenvironment (TME) and can predict diverse molecular signatures, including immune checkpoint protein expression and homologous recombination deficiency (HRD). Our HIF-based approach provides a novel, quantitative, and interpretable window into the composition and spatial architecture of the TME.

✉ Correspondence: andy.beck@pathai.com

Introduction

While manual microscopic inspection of histopathology slides remains the gold standard for evaluating the malignancy, subtype, and treatment options for cancer¹, pathologists and oncologists increasingly rely on molecular assays to guide personalization of cancer therapy². These assays can be expensive and time-consuming³, and unlike histopathology images, have not been historically and routinely collected, limiting their use in retrospective and exploratory research. Manual histological evaluation, on the other hand, presents several clinical challenges. Careful inspection requires significant time investment by board-certified anatomic pathologists and is often insufficient for prognostic prediction. Several evaluative tasks, including diagnostic classification, have also reported low inter-rater agreement

across experts and low intra-rater agreement across multiple reads by the same expert^{4,5}.

Modern computer vision methods present the potential for rapid, reproducible, and cost-effective clinical and molecular predictions. Over the past decade, the quantity and resolution of digitized histology slides has dramatically improved⁶. At the same time, the field of computer vision has made significant strides in pathology image analysis, including automated prediction of tumor grade⁷, mutational subtypes⁸, and gene expression signatures across cancer types^{9,10}. In addition to achieving diagnostic sensitivity and specificity metrics that match or exceed those of human pathologists^{11,12}, automated computational pathology can also scale to service resource-constrained settings where few pathologists are available. As a result, there may be opportunities to integrate these technologies into the clinical workflows of developing countries¹³.

However, end-to-end deep learning models that infer outputs directly from raw images present significant risks for clinical settings, including fragility of machine learning models to dataset shift, adversarial attack, and systematic biases present in training data¹⁴⁻¹⁶. Many of these risks stem from the well-known problem of model interpretability^{17,18}. “Black-box” model predictions are difficult for users to interrogate and understand, leading to user distrust. Without reliable means for understanding when and how vulnerabilities may become failures, computational methods may face difficulty achieving widespread adoption in clinical settings^{19,20}.

One emerging solution has been the automated computation of human-interpretable image features (HIFs) to predict clinical outcomes. HIF-based prediction models often mirror the pathology workflow of searching for distinctive, stage-defining features under a microscope and offer opportunities for pathologists to validate intermediate steps and identify failure points. In addition, HIF-based solutions enable incorporation of histological knowledge and expert pixel-level annotations which increases predictive power. Studied

HIFs span a wide range of visual features, including stromal morphological structures²¹, cell and nucleus morphologies²², shapes and sizes of tumor regions²³, tissue texture²⁴, and the spatial distributions of tumor-infiltrating lymphocytes (TILs)^{25,26}.

In recent years, the relationship between the TME and patient response to targeted therapies has been made increasingly clear^{27,28}. For instance, immuno-supportive phenotypes, which exhibit greater baseline antitumor immunity and improved immunotherapy response, have been linked to the presence of TILs and elevated expression of programmed death-ligand 1 (PD-L1) on tumor-associated immune cells. In contrast, immuno-suppressive phenotypes have been linked to the presence of tumor-associated macrophages and fibroblasts, as well as reduced PD-L1 expression^{28–30}. HIF-based approaches have the potential to provide an interpretable window into the composition and spatial architecture of the TME in a manner complementary to conventional genomic approaches. While prior HIF-based studies have identified many useful feature classes, most have been limited in scope. Studies to date often involve a single cell or tissue type; none have explored features that combine both cell and tissue properties. In addition, the majority of reported HIFs have only been vetted on a single cancer type, often non-small-cell lung cancer (NSCLC).

In this research study, we present a computational pathology pipeline that can integrate high-resolution cell- and tissue-level information from WSIs to predict treatment-relevant, molecularly-derived phenotypes across five different cancer types. In doing so, we introduce a diverse collection of 607 HIFs ranging from simple cell (e.g. density of lymphocytes in cancer tissue) and tissue quantities (e.g. area of necrotic tissue) to complex spatial features capturing tissue architecture, tissue morphology, and cell-cell proximity. Notably, we demonstrate that such features can generalize across cancer types and provide a quantitative and interpretable link to specific and biologically-relevant characteristics of each TME.

Results

Dataset characteristics and fully-automated pipeline design. In order to test our approach on a diverse array of histopathology images, we obtained 2,917 hematoxylin and eosin (H&E) stained, formalin-fixed and paraffin-embedded (FFPE) WSIs from the The Cancer Genome Atlas (TCGA), corresponding to 2,634 distinct patients. These images, each scanned at either 20x or 40x magnification, represented patients with skin cutaneous melanoma (SKCM), stomach adenocarcinoma (STAD), breast cancer (BRCA), lung adenocarcinoma (LUAD), and lung squamous cell carcinoma (LUSC) from 95 distinct clinical sites. We summarize the characteristics of TCGA patients in Supplemental Table 1. To supplement the TCGA analysis cohort, we obtained 4,158 additional WSIs for the five cancer types to improve model robustness.

To maximize capture of this information, we excluded images ($n = 91/2,917$, 3.1%) if they failed basic quality control checks as determined by expert pathologists. Criteria for

quality control were limited to mislabeling of tissue, excessive blur, or insufficient staining. For both TCGA and additional WSIs, we collected cell- and tissue-level annotations from a network of pathologists, amounting to >1.4 million cell-type point annotations and >200 thousand tissue-type region annotations (Supplemental Table 2).

We used the resulting slides and annotations to design a fully automated pipeline to extract HIFs from these slides (summarized in Figure 1a). First, we trained deep learning models for cell detection (“cell-type models”) and tissue region segmentation (“tissue-type models”). Training and validation of models was conducted on a development set of 1,561 TCGA WSIs, supplemented by the 4,158 additional WSIs ($n = 5719$) (Figure 1b). Next, we exhaustively generated cell- and tissue-type model predictions for 2,826 TCGA WSIs, which were then used to compute a diverse array of HIFs for each WSI. Finally, we trained classical linear machine learning models to predict treatment-relevant molecular expression phenotypes using these HIFs.

Cell- and tissue-type predictions yield a wide spectrum of HIFs.

In the first step of our pipeline, we trained two convolutional neural networks (CNNs) per cancer type: (1) tissue-type models trained to segment cancer tissue, cancer-associated stroma, and necrotic tissue regions, and (2) cell-type models trained to detect lymphocytes, plasma cells, fibroblasts, macrophages, and cancer cells. These models were improved iteratively through a series of quality control steps, including significant input from board-certified pathologists (Methods). These CNNs were then used to exhaustively generate cell-type labels and tissue-type segmentations for each WSI. We visualized these predictions as colored heatmaps projected onto the original WSIs (Figure 1c; Supplemental Figure 1). When quantified, these predictions capture broad multivariate information about the spatial distribution of cells and tissues in each slide.

Specifically, we used model predictions to extract 607 HIFs (Figure 2), which can be understood in terms of six categories (Figure 3). The first category includes cell type counts and densities across different tissue regions (e.g. density of plasma cells in cancer tissue) (Figure 3i-ii). The next category includes cell-level cluster features that capture inter-cellular spatial relationships, such as cluster dispersion, size, and extent (e.g. mean cluster size of fibroblasts in cancer-associated stroma) (Figure 3iii-iv). The third category captures cell-level proportion and proximity features, such as the proportional count of lymphocytes versus fibroblasts within 80 microns of the cancer-stroma interface (CSI) (Figure 3v-vi). The fourth category includes tissue area (e.g. mm^2 of necrotic tissue) and multiplicity counts (e.g. number of significant regions of cancer tissue) (Figures Figure 3vii-viii). The fifth category includes tissue architecture features, such as the average solidity (“solidness”) of cancer tissue regions or the fractal dimension (geometrical complexity) of cancer-associated stroma (Figures Figure 3ix-x). The final category captures tissue-level morphology using metrics such as perimeter² over area (shape roughness), lacunarity (“gappiness”), and eccentricity (Figure 3xi-xii). This broad enumer-

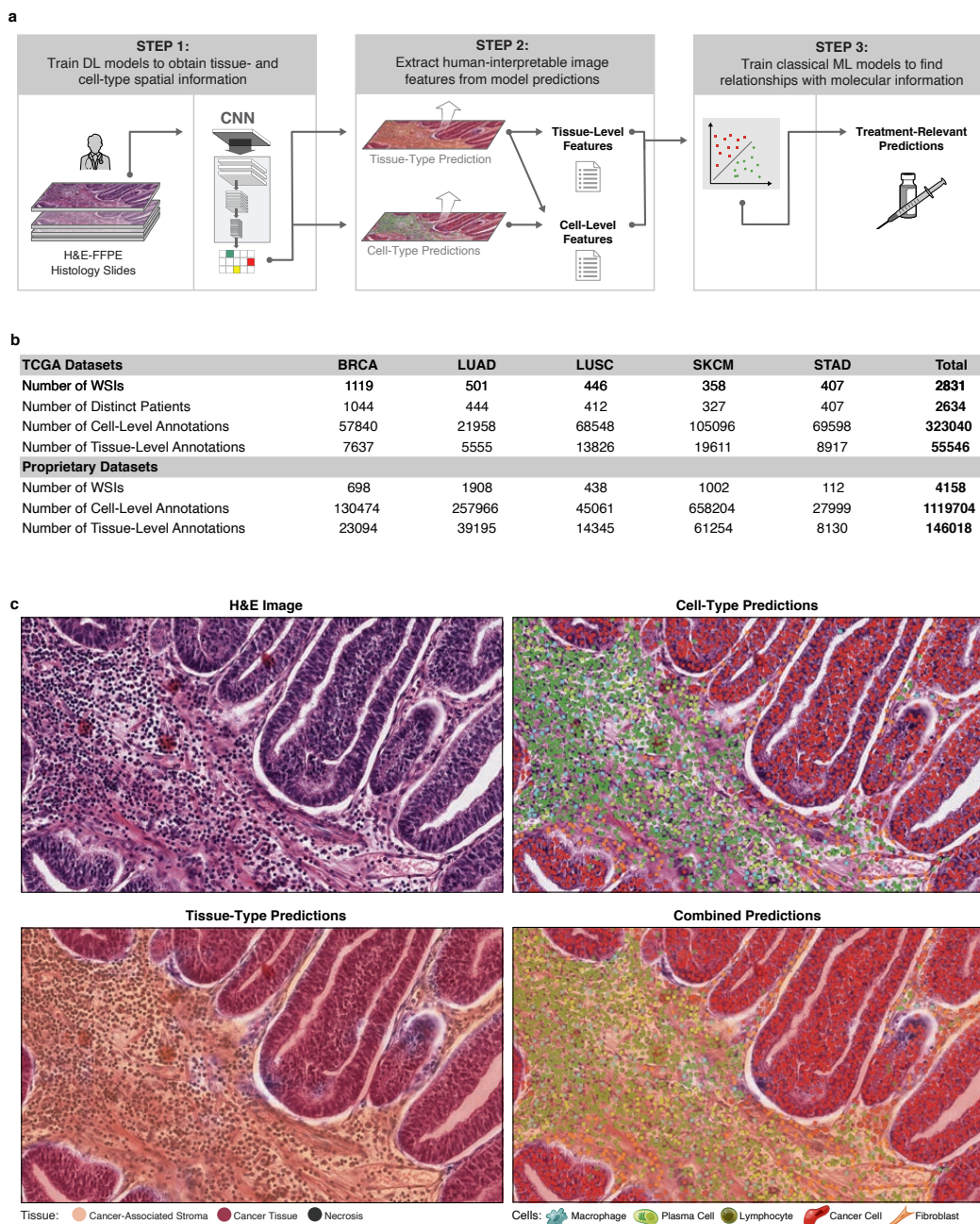


Fig. 1. Dataset and pipeline overview. a) Methodology for extracting HIFs from high-resolution, digitized H&E images. b) Summary statistics on the number of WSIs, distinct patients, and annotations curated from TCGA and additional datasets. c) Unprocessed portions of STAD H&E-stained slides alongside corresponding heatmap visualizations of cell- and tissue-type predictions. Slide regions are classified into tissue types: cancer tissue (red), cancer-associated stroma (orange), necrosis (black), or normal (transparent). Pixels in cancer tissue or cancer-associated stroma areas are classified into cell types: lymphocyte (green), plasma cell (lime), fibroblast (orange), macrophage (aqua), cancer cell (red), or background (transparent).

ation of biologically-relevant HIFs explores a wide range of mechanisms underlying histopathology across diverse cancer types.

HIFs capture sufficient information to stratify cancer types. To visualize the global structure of the HIF feature matrix, we used Uniform Manifold Approximation and Projection (UMAP) to reduce the 607-dimensional HIF space into two dimensions (Figure 4a). The 2-D manifold projection of HIFs was able to separate BRCA, SKCM, and STAD

into distinct clusters, while merging NSCLC subtypes LUAD and LUSC into one overlapping cluster (V-measure score = 0.47 using k-means with $k = 4$).

Cancer type differences could be traced to specific and interpretable cell- and tissue-level features within the TME (Figure 4b). SKCM samples exhibited higher densities of cancer cells in cancer-associated stroma (pan-cancer median Z-score = 0.55, $P < 10^{-30}$) and greater cancer tissue area per slide (Z-score = 0.72, $P < 10^{-30}$) relative to other cancer types. These findings reflect biopsy protocols for SKCM, in

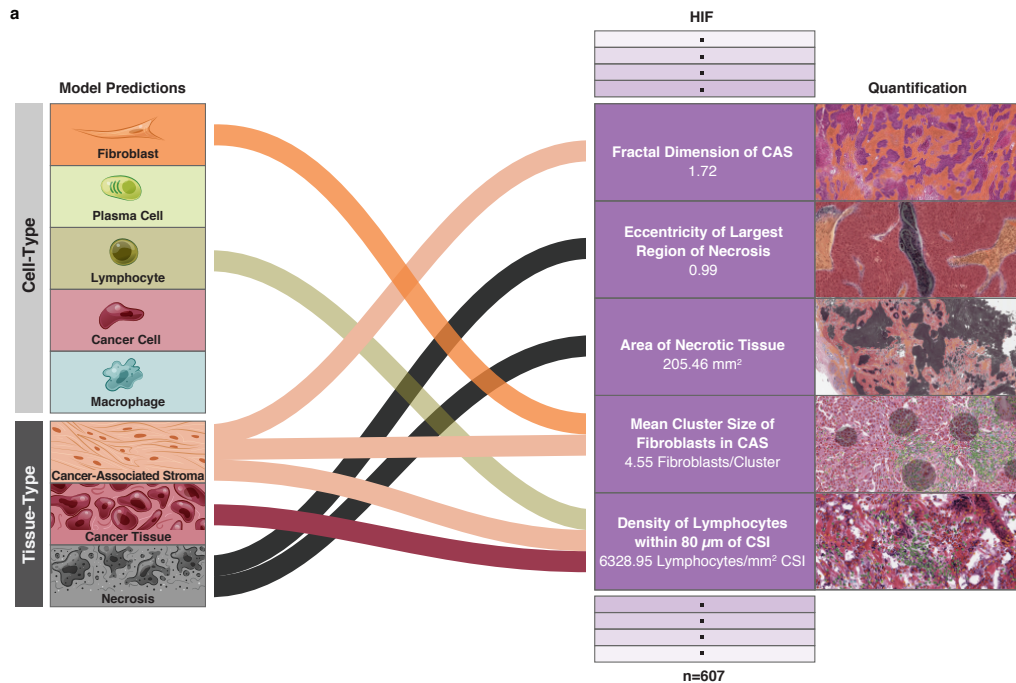


Fig. 2. Human-interpretable image feature extraction workflow. Flow diagram of HIF extraction from model predictions for five example HIFs. For each HIF, an H&E snapshot with the corresponding cell- or tissue-type heatmap overlaid and the associated quantity are shown.

which the excised region involves predominantly cancer tissue and minimal normal tissue. NSCLC subtypes LUAD and LUSC exhibited higher densities of macrophages in cancer-associated stroma (Z-score = 0.54 and 0.91, respectively; $P < 10^{-30}$), reflecting the large population of macrophages infiltrating alveolar and interstitial compartments during lung inflammation³¹. NSCLC subtypes also exhibited higher densities of plasma cells (Z-score = 0.61 and 0.49; $P < 10^{-30}$) in cancer-associated stroma, in agreement with prior findings in which proliferating B cells were observed in 35% of lung cancers^{32,33}. STAD exhibited the highest density of lymphocytes in cancer-associated stroma (Z-score = 0.11, $P = 2.16 \times 10^{-19}$), corroborating prior work which identified STAD as having the largest fraction of TIL-positive patches per WSI among thirteen TCGA cancer types, including the five examined here²⁵. Notably, HIFs are able to stratify cancer types by known histological differences without explicit tuning for cancer type detection.

HIFs are concordant with sequencing-based cell and immune marker quantifications.

To further validate our deep learning-based cell quantifications, we compared the abundance of the same cell type predicted by our cell-type models with those based on RNA sequencing³⁴. Image-based cell quantifications were correlated with sequencing-based quantifications across all patient samples and cancer types (pan-cancer) in three cell types (Supplemental Figure 2): leukocyte fraction (Spearman correlation coefficient (ρ) = 0.55, $P < 2.2 \times 10^{-16}$), lymphocyte fraction (ρ = 0.42, $P < 2.2 \times 10^{-16}$), and plasma cell fraction (ρ = 0.40, $P < 2.2 \times 10^{-16}$). Notably, imperfect correlation is expected as tissue samples used for RNA sequencing and histology imag-

ing are extracted from different portions of the patient's tumor, and thus vary in TME due to spatial heterogeneity.

There is significant correlation structure among individual HIFs due to the modular process by which feature sets are generated, as well as inherent correlations in underlying biological phenomena. For example, proportion, density, and spatial features of a given cell or tissue type all rely on the same underlying model predictions. In order to identify mechanistically-relevant and inter-correlated groups of HIFs, hierarchical agglomerative clustering was conducted (Methods; Supplemental Data 1). This clustering also increases the power of multiple-hypothesis-testing corrections by accounting for feature correlation³⁵. Pan-cancer HIF clusters strongly correlated with immune markers of leukocyte infiltration, IgG expression, TGF- β expression, and wound healing (Figure 5a), each quantified by scoring bulk RNA sequencing reads for known immune expression signatures. We conducted the same correlational analysis for each cancer type individually, and observed high concordance among the top-correlated HIF clusters per immune marker (Supplemental Table 3).

Molecular quantification of leukocyte infiltration was concordant with the density of leukocyte-lineage cells in cancer tissue plus cancer-associated stroma (CT+CAS) quantified by our deep learning pipeline, including lymphocytes (median absolute Spearman correlation ρ for associated HIF cluster = 0.48, $P < 10^{-30}$; Figure 5bi), plasma cells (cluster ρ = 0.46, $P < 10^{-30}$), and macrophages (cluster ρ = 0.40, $P < 10^{-30}$). Similarly, we observed associations between IgG expression and the density of leukocyte-lineage cells in CT+CAS, with plasma cells being the most strongly correlated (cluster ρ = 0.58, $P < 10^{-30}$), as expected given their

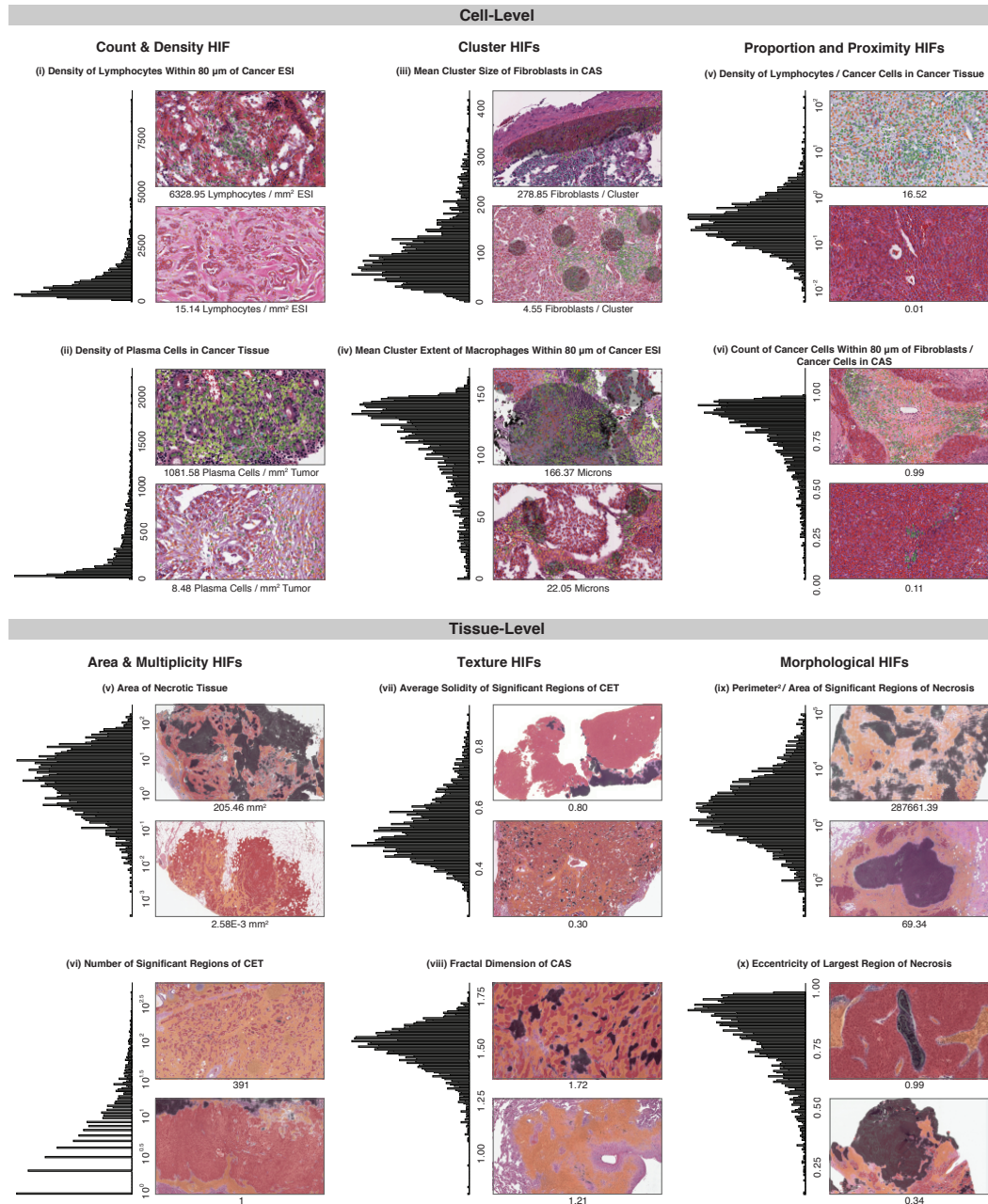


Fig. 3. Overview of HIFs. Graphical overview of the 607 HIFs grouped into six categories: cell-level count and density ($n = 56$ HIFs), cell-level cluster ($n = 180$), cell-level proportion and proximity ($n = 208$), tissue-level area and multiplicity ($n = 13$), tissue-level architecture ($n = 25$), and tissue-level morphology ($n = 125$). For each HIF, a histogram of the HIF quantified in all patient samples across the five cancer types and H&E snapshots corresponding to high and low values with the corresponding heatmap are shown. Both snapshots are taken from patient samples of the same cancer type. Cell- and tissue-type heatmaps adhere to the same color scheme described in Figure 1c. In (iii), fibroblast clusters are annotated, contrasting one large cluster against multiple smaller clusters. In (iv), macrophage clusters and extents are annotated. Cluster extent is defined as the maximum distance between a cluster exemplar (defined via Birch clustering) and a cell within that cluster. Significant regions (vii) are defined as connected components (identified at the pixel-level) of a given tissue type with at least 10% the size of the largest connected component in the slide. A solidity (ix) of one corresponds to a completely filled object, while values less than one correspond to objects containing holes or with irregular boundaries. Fractal dimension (x) can efficiently estimate the geometrical complexity and irregularity of shapes and patterns, thus capturing tissue architecture. A fractal dimension of one corresponds to a perfectly smooth tissue border, while higher fractal dimension corresponds to increasing roughness and irregularity, indicating more extensive physical contact between adjacent tissue types. The fractal dimension of the CSI has been previously associated with dysfunction in antigen presentation²⁶. Perimeter² / Area (xi) is a unitless measure of shape roughness (e.g. square = 16, circle = 4π). Across all HIFs, tumor regions include cancer tissue (CT), cancer-associated stroma (CAS), and a combined CT+CAS.

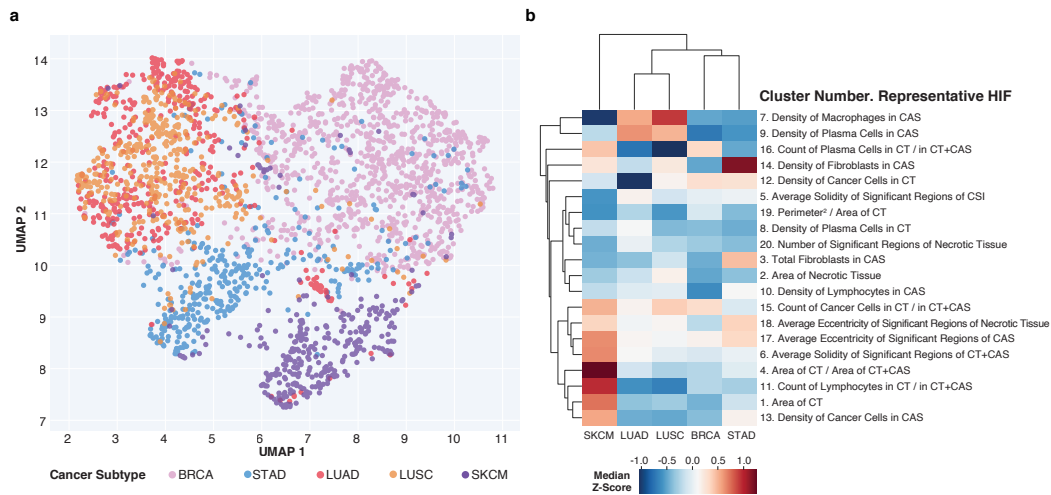


Fig. 4. HIF differences across cancer types. a) UMAP projection and visualization of five cancer types reduced from the 607-dimension HIF space into two dimensions. Each point represents a patient sample colored by cancer type. b) Clustered heatmap of median Z-scores (computed pan-cancer) across cancer types for twenty HIFs, each representing one HIF cluster (defined pan-cancer). Hierarchical clustering was performed using average linkage and Euclidean distance. Clusters are annotated with representative HIF chosen based on interpretability and high variance across cancer types.

role in producing immunoglobulins (Figure 5bii). TGF- β expression was associated with the density of fibroblasts in CT+CAS (cluster $\rho = 0.28$, $P < 10^{-30}$; Figure 5biii), building upon prior studies which found that TGF- β 1 can promote fibroblast proliferation^{36–38}. TGF- β expression was also correlated with the area of cancer-associated stroma relative to CT+CAS (cluster $\rho = 0.31$, $P < 10^{-30}$), shedding further light on the role of stromal proteins in modulating TGF- β levels³⁹. Wound healing signature was positively associated with the density of fibroblasts in cancer-associated stroma versus in cancer tissue (cluster $\rho = 0.29$, $P < 10^{-30}$; Figure 5biv), which corroborates findings that both tumors and healing wounds alike modulate fibroblast recruitment and proliferation to facilitate extracellular matrix deposition⁴⁰. H&E snapshots corresponding to high expression of each of the four immune markers are shown in Figure 5c with corresponding cell-type heatmaps overlaid.

HIFs are predictive of clinically-relevant phenotypes.

To evaluate the capability of HIFs to predict expression of clinically-relevant, immuno-modulatory genes, we conducted supervised prediction of binarized classes for five clinically-relevant phenotypes: (1) programmed cell death protein 1 (PD-1) expression, (2) PD-L1 expression, (3) cytotoxic T-lymphocyte-associated protein 4 (CTLA-4) expression, (4) HRD score, and (5) T cell immunoreceptor with Ig and ITIM domains (TIGIT) expression (Figure 6; Supplemental Figure 3). Using the 607 HIFs computed per WSI, predictions were conducted for cancer types individually as well as pan-cancer. SKCM predictions were conducted only for TIGIT expression due to insufficient sample sizes for the remainder of outcomes (Methods). To demonstrate model generalizability across varying patient demographics and sample collection processes, area under the receiver operating characteristic (AUROC) and area under the precision-recall curve (AUPRC) performance metrics were computed on hold-out sets composed exclusively of patient

samples derived from tissue source sites not seen in the training sets (Supplemental Table 4).

HIF-based models were not predictive for every phenotype in each cancer type (hold-out AUROC < 0.6 ; see Supplemental Table 5 for all results including negatives). In the successful prediction models (hold-out AUROC range = 0.601–0.864; Figure 6a), precision-recall curves revealed that models were robust to class-imbalance, achieving AUPRC performance surpassing positive class prevalence by 0.104–0.306 (Supplemental Figure 4). Notably, AUROC performance of our HIF-based linear model for PD-L1 expression in LUAD was comparable to that achieved by “black-box” deep learning models trained on hundreds of thousands of paired H&E and PD-L1 example patches in NSCLC⁴¹.

Predictive HIFs provide interpretable link to clinically-relevant phenotypes.

Interpretable features enable interrogation and further validation of model parameters as well as generation of new biological hypotheses. Towards this end, for each prediction task we identified the five most important HIF clusters as determined by magnitude of model coefficients (Figure 6b; Supplemental Figure 5) and computed cluster-level P-values to evaluate significance (Supplemental Table 6; Methods).

As expected, prediction of PD-1 and PD-L1 involved similar HIF clusters (Pearson correlation between PD-1 and PD-L1 expression = 0.53; Supplemental Figure 6). The count of cancer cells within 80 microns of lymphocytes, as well as the density of lymphocytes in CT+CAS, was significantly selected during model fitting for both of PD-1 and PD-L1 expression in pan-cancer and BRCA models (Figure 6bi-ii; Supplemental Figures 5i-ii). Furthermore, in both LUAD and LUSC, the count of lymphocytes in CT+CAS was similarly predictive of PD-1 and PD-L1 expression. The importance of these HIFs which capture lymphocyte infiltration between and surrounding cancer cells corroborates prior literature which demonstrated that TILs correlated strongly with

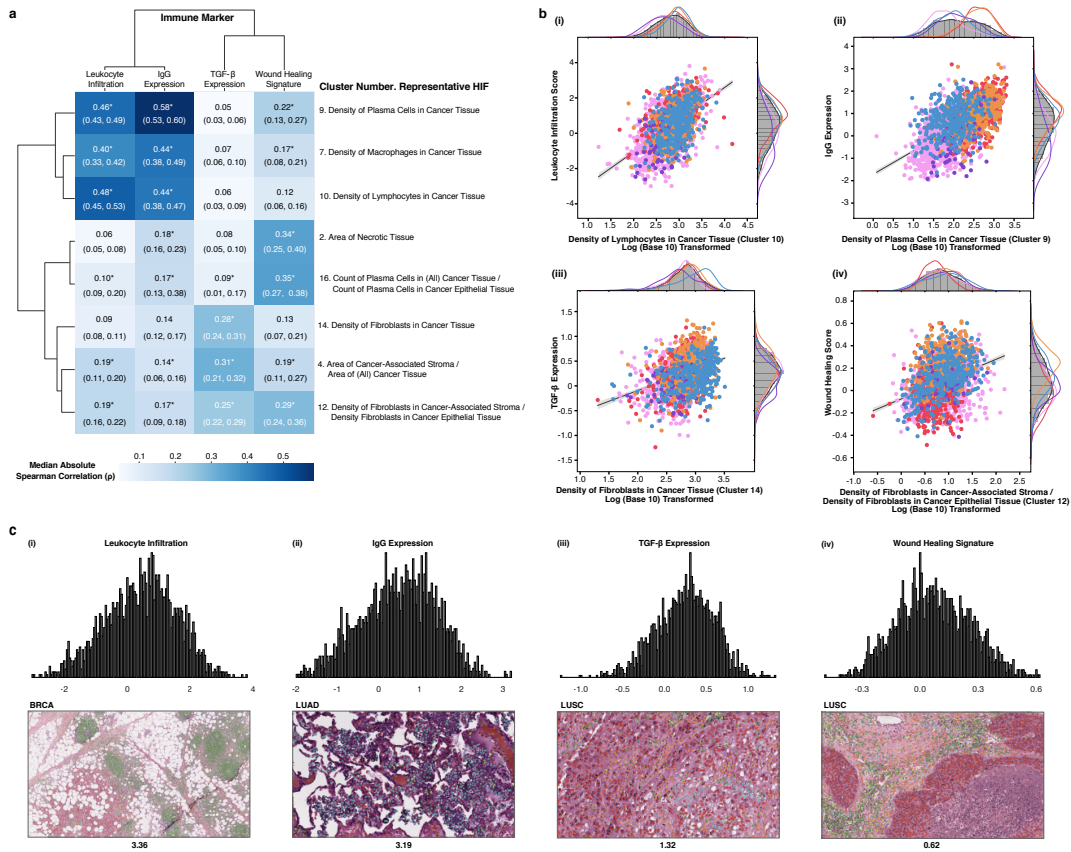


Fig. 5. Validation of HIFs against immune markers. a) Clustered heatmap of median absolute Spearman correlation coefficients (ρ) computed across all patient samples between eight HIF clusters (defined pan-cancer) and four canonical immune markers. Hierarchical clustering was done using average linkage and euclidean distance. Median absolute Spearman correlation coefficients with a combined (via the Empirical Brown's method) and corrected (via the Benjamini-Hochberg procedure) P value lower than the machine precision level (10^{-30}) are annotated with an asterisk. Negative control analyses are included in Supplemental Table 3. Tumor regions include cancer tissue (CT), cancer-associated stroma (CAS), and a combined CT+CAS. b) Correlation and kernel density estimation plots between representative HIFs and immune markers. Points are colored by cancer type. X-axes are log-transformed (base ten). Trendlines are plotted on the log-transformed data. Cell densities are reported in count/mm² and tissue areas are reported in mm². c) Histogram of immune marker expression (Z-score) across all patients, alongside an H&E snapshot with its cell-type heatmap overlaid corresponding to high expression of the given immune marker. Cell-type heatmaps adhere to the same color scheme described in Figure 1c.

higher expression levels of PD-1 and PD-L1 in early breast cancer⁴² and NSCLC^{43,44}.

The area, morphology, or multiplicity of necrotic tissue proved predictive of PD-1 expression in LUAD, LUSC, and STAD models and of PD-L1 expression in pan-cancer, BRCA, and LUAD models, expanding upon prior findings that tumor necrosis correlated positively with PD-1 and PD-L1 expression in LUAD⁴⁵. The density, proximity, or clustering properties of plasma cells was predictive of PD-1 expression in all models excluding LUAD, suggesting a role for plasma cells in modulating PD-1 expression. Recent studies in SKCM, renal cell carcinoma, and soft-tissue sarcoma have demonstrated that an enrichment of B-cells in tertiary lymphoid structures was positively predictive of response to immune checkpoint blockade therapy⁴⁶⁻⁴⁸. The density of fibroblasts in cancer-associated stroma or within 80 microns of the CSI was predictive of PD-L1 expression in LUAD and STAD, respectively, corroborating earlier discoveries that cancer-associated fibroblasts promote PD-L1 expression⁴⁹.

Less is known about the relationship between the TME and CTLA-4 expression. By investigating predictive HIFs we can begin to enumerate features of the TME that corre-

late with CTLA-4 expression. The proximity of lymphocytes to cancer cells (pan-cancer and BRCA), morphology of necrotic regions (LUAD and LUSC), and density of cancer cells in CT+CAS versus exclusively in cancer-associated stroma (BRCA and STAD) were predictive of CTLA-4 expression across multiple models (Figure 6biii; Supplemental Figure 5iii).

Area of necrotic tissue (pan-cancer and BRCA) as well as various morphological properties of necrotic regions including perimeter and lacunarity (BRCA and STAD) were predictive of HRD (Figure 6biv; Supplemental 5iv). In HRD, ineffective DNA damage repair can result in the accumulation of severe DNA damage and subsequent cell death through apoptosis as well as necrosis^{50,51}. The density and count of fibroblasts near or in cancer-associated stroma was also predictive of HRD in the pan-cancer and BRCA models, corroborating prior findings that persistent DNA damage and subsequent accumulation of unrepaired DNA strand breaks can induce reprogramming of normal fibroblasts into cancer-associated fibroblasts⁵².

Like the three other immune checkpoint proteins (PD-1, PD-L1, and CTLA-4), TIGIT expression was also associated with markers of tumor inflammation, including the

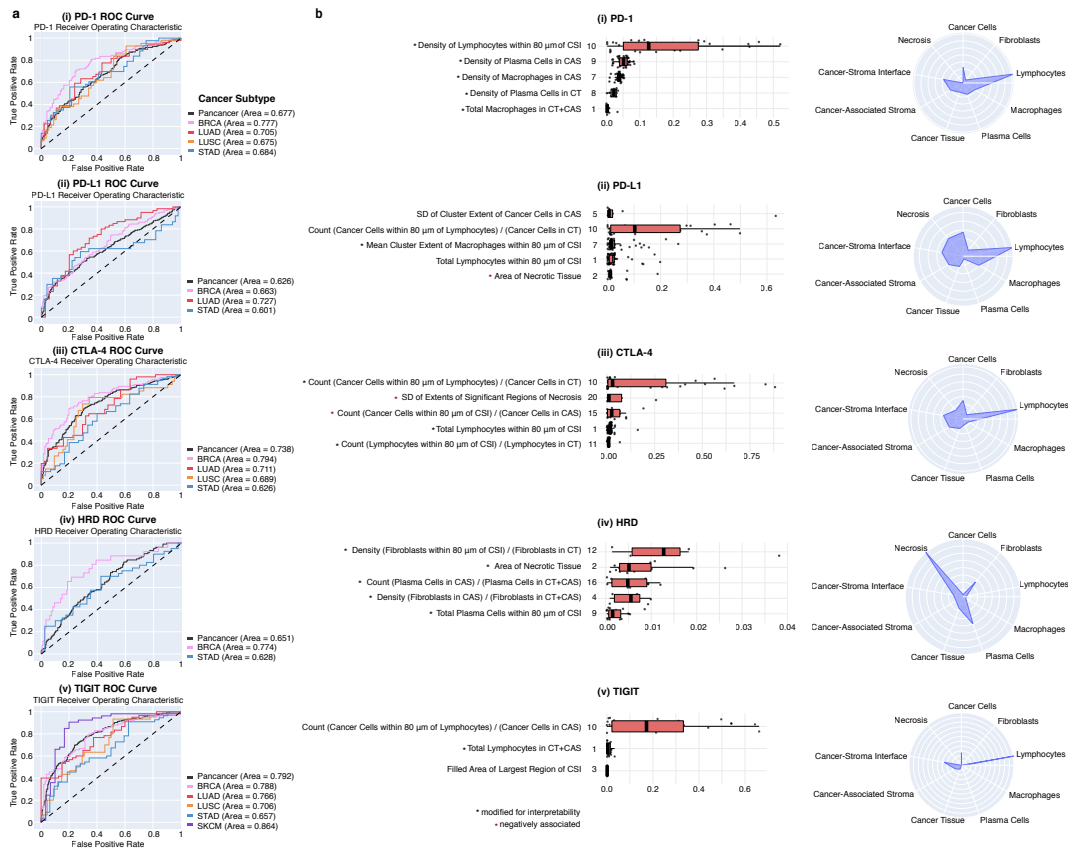


Fig. 6. HIF-based prediction of molecular phenotypes. a) ROC curves for (i) PD-1, (ii) PD-L1, (iii) CTLA-4, (iv) HRD, and (v) TIGIT hold-out predictions across cancer types and pan-cancer. SKCM predictions were conducted only for TIGIT due to low sample sizes. Pan-cancer predictions use binary labels thresholded independently by cancer type. For TIGIT predictions, pan-cancer includes all five cancer types. For the remainder of predictions, pan-cancer includes all cancer types excluding SKCM. Random classifiers correspond to AUROC = 0.50. b) Visualization of predictive HIFs for each molecular phenotype. Boxplots show the top five most predictive HIF clusters for each phenotype in pan-cancer models. For TIGIT predictions, pan-cancer models only included three non-zero HIF clusters. Clusters are ranked by the maximum absolute ensemble beta across HIFs in a given cluster. Ensemble betas are computed per HIF as the average across the three models incorporated into the final ensemble evaluated on the hold-out set. Each boxplot highlights the median and interquartile range for ensemble betas in each cluster. Each cluster is labeled with a representative HIF corresponding to the maximum absolute ensemble beta value. In cases where that HIF is difficult to interpret, a more interpretable HIF within a five-fold difference of the maximum ensemble beta is presented (indicated by a black asterisk). As absolute values were used for ranking, HIFs with negative ensemble betas are denoted by a red asterisk. Boxplots of predictive HIF clusters for cancer type-specific models are included in Supplemental Figure 5. Radar charts show the normalized magnitude of ensemble betas in pan-cancer models stratified across nine HIF axes, corresponding to the five cell types, three tissue types, and CSI. Normalized magnitudes were computed as the sum of absolute ensemble betas for HIFs associated with each axis divided by the total number of HIFs associated with said axis (e.g. all HIFs involving fibroblasts). Multiple predictive HIFs are visualized with overlaid cell- or tissue-type heatmaps in Figure 3. Tumor regions include cancer tissue (CT), cancer-associated stroma (CAS), and a combined CT+CAS.

count of cancer cells within 80 microns of lymphocytes (pan-cancer and BRCA), the total number of lymphocytes in CT+CAS (pan-cancer and BRCA), and the proportional count of lymphocytes to cancer cells within 80 microns of the CSI (LUAD) (Figure 6bv; Supplemental Figure 5v). These findings corroborate prior findings that TIGIT expression, alongside PD-1 and PD-L1 expression (Pearson correlation between TIGIT and PD-1 = 0.84; TIGIT and PD-L1 = 0.56; Supplemental Figure 6), is correlated with TILs⁵³. HIF clusters capturing morphology and architecture of necrotic tissue (e.g. fractal dimension, lacunarity, extent, perimeter² / area) were associated with TIGIT expression in LUAD, LUSC, SKCM, and STAD models, although these relationships have yet to be investigated.

Discussion

Our study is the first to demonstrate the value of combining deep learning-based cell- and tissue-type classifications

to compute image features that are both biologically-relevant and human-interpretable. We demonstrate that computed HIFs can recapitulate sequencing-based cell quantifications, capture canonical immune markers such as leukocyte infiltration and TGF- β expression, and robustly predict five molecular phenotypes relevant to oncology treatment efficacy and response. We also demonstrate the generalizability of our associations, as evidenced by similarly predictive HIF clusters across biopsy images derived from five different cancer types. While prior studies have applied deep learning methodologies to capture cell-level information, such as the spatial configuration of immune and stromal cells^{26,54}, or tissue-level information⁵⁵ alone, our combined cell plus tissue approach enables quantification of increasingly complex and expressive features of the TME, ranging from the mean cluster size of fibroblasts in cancer-associated stroma to the proximity of TILs or cancer-associated fibroblasts to the CSI. By training models to make six-class cell-type and four-class tissue-

type classifications, our approach is also able to aggregate more layers of information than prior studies. Indeed, while TILs are emerging as a promising biomarker in solid tumors such as triple-negative and HER2-positive breast cancer⁵⁴, TILs differ from stromal lymphocytes, and substantial signal can be obtained by considering multiple cell-tissue combinations²¹.

Our approach of exhaustively generating cell- and tissue-type predictions across entire WSIs at subcellular resolution (of two and four microns, respectively) is novel to the best of our knowledge, and improves upon previous tiling approaches that downsample the image. The tissue visible in a WSI is already only a fraction of the tumor itself. Using the entire slide (rather than selected tiles) reduces the probability of fixating on non-generalizable local effects and enables quantification of complex characteristics that span multiple tissue regions (e.g. multiplicity, solidity, and fractal dimension of significant necrotic regions).

In addition, our approach of capturing specific and interpretable features of the tumor and its surroundings can facilitate hypothesis generation and enable a deeper understanding of the TME's influence on drug response. Indeed, recent studies provide evidence that tumor immune architecture can greatly dictate clinical efficacy of immune checkpoint inhibitor⁵⁶ and poly (ADP-ribose) polymerase (PARP) inhibitor therapies⁵⁷.

Lastly, during both model development and evaluation, we sought to emphasize robustness to real-world variability⁵⁸. In particular, we supplemented TCGA WSIs with additional diverse datasets during CNN training, integrated pathologist feedback into model iterations, and evaluated HIF-based model performance on hold-out sets composed exclusively of samples from unseen tissue source sites, improving upon prior approaches to predicting molecular outcomes from TCGA H&E images^{22,59}.

One major limitation of machine-learning approaches is the quality of training data. While our cell and tissue classification models were trained on a combination of TCGA and additional datasets, molecular associations and predictions were derived solely from TCGA. Biopsy images submitted to the TCGA dataset suffer from selection bias towards more definitive diagnoses and early-stage disease that may not generalize well to ordinary clinical settings. Moreover, the images only contain H&E staining, which limits the amount of information available to us. It is possible that integrating multimodal data containing stains against Ki-67 or immunohistological targets may increase confidence in cell classifications⁶⁰. In addition to the quality of slide images, annotations are also variable in reliability. Macrophages are particularly difficult for pathologists to identify solely under H&E staining. While the accuracy of an individual pathologist identifying macrophages may be poor, our models represent a consensus across hundreds of pathologist annotators which may carry a more reliable signal^{61,62}.

Furthermore, morphologically similar cells (e.g. macrophages, dendritic cells, endothelial cells, pericytes, myeloid derived suppressor cells, and atypical lymphocytes)

may all be captured under a single cell-type prediction. Thus, HIFs may, in reality, capture information about a mixture of cell types. For example, in diffuse forms of STAD in which cancer cells invade smooth muscle tissue, our models misclassified certain smooth muscle cells as fibroblasts. Therefore, fibroblast-label HIFs likely reflect a mixture of these two cell types in STAD. Further disambiguation of morphologically-similar cell types may decrease noise in HIF estimates and improve performance.

These interpretable sets of HIFs, computed from tens-of-thousands of deep learning-based cell- and tissue-type predictions per patient, improve upon conventional "black-box" approaches which apply deep learning directly to WSIs, yielding models with millions of parameters and limited interpretability. Recent work has revealed the weaknesses of low-interpretability models, including brittleness to dataset shift, vulnerabilities to adversarial attack, and susceptibility to the biases of the data-generative process. Unlike class activation maps utilized in prior studies as a heuristic to identify predictive image regions^{9,10}, HIFs can be interpreted in aggregate across thousands of images and mapped directly onto biological concepts.

Beyond suggesting interpretable hypotheses for causal mechanisms (e.g. the anti-tumor effect of high lymphocyte density), our HIF-based approach can be continually validated at several points: pathologists can judge the quality of cell and tissue-type predictions, estimate the values of each relevant feature using traditional manual scoring, and observe whether there is a significant failure given real-world variability in sample preparation and quality. Unlike "black-box" models that may opaquely rely on features that are predictive but disconnected from the outcome of interest, such as tissue excision or preparation artifacts (e.g. surgical or pathologist markings)^{16,19}, HIF-based predictions can be traced to observable features, allowing model failures to be explained and addressed. While performance is vitally important in clinical settings and additional studies comparing end-to-end and HIF-based approaches are needed, the improved trust and reliability against unexpected failures make HIF-based models a valuable alternative.

Finally, the ability to predict molecular phenotypes directly from WSIs in an interpretable fashion has numerous potential benefits for clinical oncology. Hospitals, healthcare institutions, and pharmaceutical and biotechnology companies have decades of archival histopathology data captured from routine care and clinical trials⁶³. HIF-based models capable of capturing molecular information could supplement molecular assays that are often expensive and time-consuming³, enable the discovery of novel patient subpopulations with specific disease processes and treatment susceptibilities, and generate hypotheses for subsequent research.

ACKNOWLEDGEMENTS

We are grateful to the software engineering and machine learning teams at PathAI, Inc. for developing the systems and pipelines used for model development and feature extraction. We also thank the Harvard-MIT Program in Health Sciences and Technology for enabling J.A.D., W.F.C., and J.K.W. to conduct this work towards satisfaction of their research theses. This work was funded by PathAI, Inc.

AUTHOR CONTRIBUTIONS

J.A.D., W.F.C., J.K.W., A.T.W., H.L.E., and A.H.B. conceived the project. J.A.D. and W.F.C. trained the models, generated heatmaps, and computed image features. A.L. and C.M. assisted with model troubleshooting and feature computation. S.K.R. and M.B.R. provided feedback on predicted heatmaps to enable iterative model improvements. B.G. and I.N.W. supervised collection of pathologist annotations for model training. J.A.D. and J.K.W. conducted statistical analysis of image feature associations. J.K.W. developed models for molecular phenotype prediction and image feature visualization. H.L.E. and A.T.W. supervised model training and statistical analyses. All authors contributed to preparation of the manuscript.

COMPETING FINANCIAL INTERESTS

The authors declare the following competing interests: A.K. and A.H.B. are the co-founders of PathAI, Inc., a company that builds artificial intelligence tools for pathology. J.A.D., W.F.C., J.K.W., S.K.R., M.B.R., A.L., C.M., B.G., V.M., J.K.K., M.C.M., I.N.W., A.T.W., and H.L.E. are currently, or were formerly, employed at PathAI, Inc.

References

1. Lei He, L Rodney Long, Sameer Antani, and George R Thoma. Histology image analysis for carcinoma detection and grading, 2012.
2. Anna P Sokolenko and Evgeny N Imyanov. Molecular diagnostics in clinical oncology. *Front Mol Biosci*, 5:76, August 2018.
3. Wafik S El-Deiry, Richard M Goldberg, Heinz-Josef Lenz, Anthony F Shields, Geoffrey T Gibney, Antoinette R Tan, Jubilee Brown, Burton Eisenberg, Elisabeth I Heath, Surasak Phuphanich, Edward Kim, Andrew J Brenner, and John L Marshall. The current state of molecular testing in the treatment of patients with solid tumors, 2019. *CA Cancer J. Clin.*, 69(4):305–343, July 2019.
4. Takeshi Yamaguchi, Hirofumi Mukai, Futoshi Akiyama, Koji Arihiro, Shinobu Masuda, Masafumi Kurosumi, Yoshinori Kodama, Rie Horii, and Hitoshi Tsuda. Inter-observer agreement among pathologists in grading the pathological response to neoadjuvant chemotherapy in breast cancer. *Breast Cancer*, 25(1):118–125, January 2018.
5. J H M J Vestjens, M J Pepels, M de Boer, G F Borrm, C H M van Deurzen, P J van Diest, J A M van Dijk, E M M Adang, J W R Nortier, E J Th Rutgers, C Seynaeve, M B E Menke-Plymvers, P Bult, and V C G Tjan-Heijnen. Relevant impact of central pathology review on nodal classification in individual breast cancer patients. *Ann. Oncol.*, 23(10):2561–2566, October 2012.
6. Sten Thorstenson, Jesper Molin, and Claes Lundström. Implementation of large-scale routine diagnostics using whole slide imaging in sweden: Digital pathology experiences 2006-2013. *J. Pathol. Inform.*, 5(1):14, March 2014.
7. Kunal Nagpal, Davis Foote, Yun Liu, Po-Hsuan Cameron Chen, Ellery Wulczyn, Fraser Tan, Niels Olson, Jenny L Smith, Arash Mohtashamian, James H Wren, Greg S Corrado, Robert MacDonald, Lily H Peng, Mahul B Amin, Andrew J Evans, Ankur R Sangoi, Craig H Mermel, Jason D Hipp, and Martin C Stumpe. Development and validation of a deep learning algorithm for improving gleason scoring of prostate cancer. *NPJ Digit Med*, 2:48, June 2019.
8. Nicolas Coudray, Paolo Santiago Ocampo, Theodore Sakellariopoulos, Navneet Narula, Matija Snuderl, David Fenyo, Andre L Moreira, Narges Razavian, and Aristotelis Tsirogos. Classification and mutation prediction from non-small cell lung cancer histopathology images using deep learning. *Nat. Med.*, 24(10):1559–1567, October 2018.
9. Jakob Nikolas Kather, Lara R Heij, Heike I Grabsch, Chiara Loeffler, Amelie Echle, Hannah Sophie Muti, Jeremias Krause, Jan M Niehues, Kai A J Sommer, Peter Bankhead, Loes F S Kooreman, Jeffrey J Schulte, Nicole A Cipriani, Roman D Buelow, Peter Boor, Nadina Ortiz-Brüchle, Andrew M Hanby, Valerie Speirs, Sara Kochanny, Akash Patnaik, Andrew Srisuwananukorn, Hermann Brenner, Michael Hoffmeister, Piet A van den Brandt, Dirk Jäger, Christian Trautwein, Alexander T Pearson, and Tom Luedde. Pan-cancer image-based detection of clinically actionable genetic alterations. *Nature Cancer*, July 2020.
10. Yu Fu, Alexander W Jung, Ramon Viñas Torne, Santiago Gonzalez, Harald Vöhringer, Artem Shmatko, Lucy R Yates, Mercedes Jimenez-Linan, Luiza Moore, and Moritz Gerstung. Pan-cancer computational histopathology reveals mutations, tumor composition and prognosis. *Nature Cancer*, July 2020.
11. Babak Ehteshami Bejnordi, Mitko Veta, Paul Johannes van Diest, Bram van Ginneken, Nico Karssemeijer, Geert Litjens, Jeroen A W M van der Laak, the CAMELYON16 Consortium, Meyke Hermens, Quirine F Manson, Maschenka Balkenhol, Oscar Geessink, Nikolaos Stathonikos, Marcoray Crf van Dijk, Peter Bult, Francisco Beca, Andrew H Beck, Dayong Wang, Aditya Khosla, Rishab Gargeya, Humayun Irshad, Aoxiao Zhong, Qi Dou, Quanzheng Li, Hao Chen, Huang-Jing Lin, Peng-Ann Heng, Christian Haß, Eli Bruni, Quincy Wong, Ugur Halici, Mustafa Ümit Öner, Rengul Cetin-Atalay, Matt Berseht, Vitali Khvatkov, Alexei Vylegzhanin, Oren Kraus, Muhammad Shaban, Nasir Rajpoot, Ruqayya Awan, Korsuk Sirinukunwattana, Talha Qaiser, Yee-Wah Tsang, David Tellez, Jonas Annuscheit, Peter Hufnagl, Mira Valkonen, Kimmo Kartasalo, Leena Latonen, Pekka Ruusu-vuori, Kaisa Liimatainen, Shadi Albarqouni, Bharti Mungal, Ami George, Stefanie Demirci, Nassir Navab, Seiryu Watanabe, Shigeto Seno, Yoichi Takenaka, Hideo Matsuda, Hady Ahmady Phoulady, Vassili Kovalev, Alexander Kalinovsky, Vitali Liauchuk, Gloria Bueno, M Milagro Fernandez-Carrobles, Ismael Serrano, Oscar Deniz, Daniel Racoceanu, and Rui Venâncio. Diagnostic assessment of deep learning algorithms for detection of lymph node metastases in women with breast cancer. *JAMA*, 318(22):2199–2210, December 2017.
12. Dayong Wang, Aditya Khosla, Rishab Gargeya, Humayun Irshad, and Andrew H Beck. Deep learning for identifying metastatic breast cancer. *arXiv*, June 2016.
13. Gabriele Campanella, Matthew G Hanna, Luke Geneslaw, Allen Miralfor, Vitor Werneck Krauss Silva, Klaus J Busam, Edi Brogi, Victor E Reuter, David S Klimstra, and Thomas J Fuchs. Clinical-grade computational pathology using weakly supervised deep learning on whole slide images. *Nat. Med.*, 25(8):1301–1309, August 2019.
14. Luke Oakden-Rayner, Jared Dunmon, Gustavo Carneiro, and Christopher Re. Hidden stratification causes clinically meaningful failures in machine learning for medical imaging.

- In *Proceedings of the ACM Conference on Health, Inference, and Learning*, CHIL '20, pages 151–159, New York, NY, USA, April 2020. Association for Computing Machinery.
15. Samuel G Finlayson, John D Bowers, Joichi Ito, Jonathan L Zittrain, Andrew L Beam, and Isaac S Kohane. Adversarial attacks on medical machine learning. *Science*, 363(6433): 1287–1289, March 2019.
 16. Julia K Winkler, Christine Fink, Ferdinand Toberer, Alexander Enk, Teresa Deinlein, Rainer Hofmann-Wellenhof, Luc Thomas, Aimiios Lallas, Andreas Blum, Wilhelm Stolz, and Holger A Haenssle. Association between surgical skin markings in dermoscopic images and diagnostic performance of a deep learning convolutional neural network for melanoma recognition. *JAMA Dermatol.*, August 2019.
 17. Travers Ching, Daniel S Himmelstein, Brett K Beaulieu-Jones, Alexandr A Kalinin, Brian T Do, Gregory P Way, Enrico Ferrero, Paul-Michael Agapow, Michael Zietz, Michael M Hoffman, Wei Xie, Gail L Rosen, Benjamin J Lengerich, Johnny Israeli, Jack Lanchantin, Stephen Woloszynek, Anne E Carpenter, Anvari Shrikumar, Jinbo Xu, Evan M Cofer, Christopher A Lavender, Srinivas C Turaga, Amr M Alexandari, Zhiyong Lu, David J Harris, Dave DeCaprio, Yanjun Qi, Anshul Kundaje, Yifan Peng, Laura K Wiley, Marwin H S Segler, Simina M Boca, S Joshua Swamidass, Austin Huang, Anthony Gitter, and Casey S Greene. Opportunities and obstacles for deep learning in biology and medicine. *J. R. Soc. Interface*, 15(141), April 2018.
 18. Anant Madabhushi and George Lee. Image analysis and machine learning in digital pathology: Challenges and opportunities. *Med. Image Anal.*, 33:170–175, October 2016.
 19. Christopher J Kelly, Alan Karthikesalingam, Mustafa Suleyman, Greg Corrado, and Dominic King. Key challenges for delivering clinical impact with artificial intelligence. *BMC Med.*, 17(1):195, October 2019.
 20. Andreas Holzinger, Chris Biemann, Constantinos S Pattichis, and Douglas B Kell. What do we need to build explainable AI systems for the medical domain? *arXiv*, December 2017.
 21. Andrew H Beck, Ankur R Sangoi, Samuel Leung, Robert J Marinelli, Torsten O Nielsen, Marc J van de Vijver, Robert B West, Matt van de Rijn, and Daphne Koller. Systematic analysis of breast cancer morphology uncovers stromal features associated with survival. *Sci. Transl. Med.*, 3(108):108ra113, November 2011.
 22. Kun-Hsing Yu, Ce Zhang, Gerald J Berry, Russ B Altman, Christopher Ré, Daniel L Rubin, and Michael Snyder. Predicting non-small cell lung cancer prognosis by fully automated microscopic pathology image features. *Nat. Commun.*, 7:12474, August 2016.
 23. Shidan Wang, Alyssa Chen, Lin Yang, Ling Cai, Yang Xie, Junya Fujimoto, Adi Gazdar, and Guanghua Xiao. Comprehensive analysis of lung cancer pathology images to discover tumor shape and boundary features that predict survival outcome. *Sci. Rep.*, 8(1):10393, July 2018.
 24. Frances E Lennon, Gianguido C Cianci, Nicole A Cipriani, Thomas A Hensing, Hannah J Zhang, Chin-Tu Chen, Septimiu D Murgu, Everett E Vokes, Michael W Vannier, and Ravi Salgia. Lung cancer—a fractal viewpoint, 2015.
 25. Joel Saltz, Rajarsi Gupta, Le Hou, Tahsin Kurb, Pankaj Singh, Vu Nguyen, Dimitris Samaras, Kenneth R Shroyer, Tianhao Zhao, Rebecca Batiste, John Van Arnam, Cancer Genome Atlas Research Network, Ilya Shmulevich, Arvind U K Rao, Alexander J Lazar, Ashish Sharma, and Vésteinn Thorsson. Spatial organization and molecular correlation of Tumor-Infiltrating lymphocytes using deep learning on pathology images. *Cell Rep.*, 23(1):181–193.e7, April 2018.
 26. Khalid Abduljabbar, Shan E Ahmed Raza, Rachel Rosenthal, Mariam Jamal-Hanjani, Selvaraju Veeriah, Ayse Akarca, Tom Lund, David A Moore, Roberto Salgado, Maise Al Bakir, Luis Zapata, Crispin T Hiley, Leah Officer, Marco Sereno, Claire Rachel Smith, Shereene Loi, Allan Hackshaw, Teresa Marafioti, Sergio A Quezada, Nicholas McGranahan, John Le Quesne, TRACERx Consortium, Charles Swanton, and Yinyin Yuan. Geospatial immune variability illuminates differential evolution of lung adenocarcinoma. *Nat. Med.*, May 2020.
 27. Wolf H Fridman. The immune microenvironment as a guide for cancer therapies. *Oncoimmunology*, 1(3):261–262, May 2012.
 28. Jérôme Galon and Daniela Bruni. Approaches to treat immune hot, altered and cold tumours with combination immunotherapies. *Nat. Rev. Drug Discov.*, 18(3):197–218, March 2019.
 29. Yibing Chen, Yucen Song, Wei Du, Longlong Gong, Haocai Chang, and Zhengzhi Zou. Tumor-associated macrophages: an accomplice in solid tumor progression. *J. Biomed. Sci.*, 26(1):78, October 2019.
 30. Jieying Zhang, Zhaopeng Shi, Xiang Xu, Zuoren Yu, and Jun Mi. The influence of microenvironment on tumor immunotherapy. *FEBS J.*, 286(21):4160–4175, November 2019.
 31. Guochang Hu and John W Christman. Editorial: Alveolar macrophages in lung inflammation and resolution. *Front. Immunol.*, 10:2275, September 2019.
 32. Si-Si Wang, Wei Liu, Dalam Ly, Hao Xu, Limei Qu, and Li Zhang. Tumor-infiltrating B cells: their role and application in anti-tumor immunity in lung cancer. *Cell. Mol. Immunol.*, 16(1): 6–18, January 2019.
 33. Elizabeth B Gottlin, Rex C Bentley, Michael J Campa, David S Pisetsky, James E Herndon, 2nd, and Edward F Patz, Jr. The association of intratumoral germinal centers with early-stage non-small cell lung cancer. *J. Thorac. Oncol.*, 6(10):1687–1690, October 2011.
 34. Aaron M Newman, Chih Long Liu, Michael R Green, Andrew J Gentles, Weiguo Feng, Yue Xu, Chuong D Hoang, Maximilian Diehn, and Ash A Alizadeh. Robust enumeration of cell subsets from tissue expression profiles. *Nat. Methods*, 12(5):453–457, May 2015.
 35. William Poole, David L Gibbs, Ilya Shmulevich, Brady Bernard, and Theo A Knijnenburg. Combining dependent p-values with an empirical adaptation of brown's method. *Bioinformatics*, 32(17):i430–i436, September 2016.
 36. Ying Liu, Yue Li, Ning Li, Wen Teng, Min Wang, Yingbo Zhang, and Zhibo Xiao. TGF- β 1 promotes scar fibroblasts proliferation and transdifferentiation via up-regulating MicroRNA-21. *Sci. Rep.*, 6:32231, August 2016.
 37. Petrov Victor V, Fagard Robert H., and Lijnen Paul J. Stimulation of collagen production by transforming growth Factor- β 1 during differentiation of cardiac fibroblasts to myofibroblasts. *Hypertension*, 39(2):258–263, February 2002.
 38. Dulce Maroni and John S Davis. Transforming growth factor beta 1 stimulates profibrotic activities of luteal fibroblasts in cows. *Biol. Reprod.*, 87(5):127, November 2012.
 39. Brunella Costanza, Ijeoma Adaku Umelo, Justine Bellier, Vincent Castronovo, and Andrei Turtoi. Stromal modulators of TGF- β in cancer. *J. Clin. Med. Res.*, 6(1), January 2017.

40. Deshka S Foster, R Ellen Jones, Ryan C Ransom, Michael T Longaker, and Jeffrey A Norton. The evolving relationship of wound healing and tumor stroma. *JCI Insight*, 3(18), September 2018.
41. Lingdao Sha, Boleslaw L Osinski, Irvin Y Ho, Timothy L Tan, Caleb Willis, Hannah Weiss, Nike Beaubier, Brett M Mahon, Tim J Taxter, and Stephen S F Yip. Multi-Field-of-View deep learning model predicts nonsmall cell lung cancer programmed Death-Ligand 1 status from Whole-Slide hematoxylin and eosin images. *J. Pathol. Inform.*, 10:24, July 2019.
42. Atsuko Kitano, Makiko Ono, Masayuki Yoshida, Emi Noguchi, Akihiko Shimomura, Tatsunori Shimoi, Makoto Kodaira, Mayu Yunokawa, Kano Yonemori, Chikako Shimizu, Takayuki Kinoshita, Yasuhiro Fujiwara, Hitoshi Tsuda, and Kenji Tamura. Tumour-infiltrating lymphocytes are correlated with higher expression levels of PD-1 and PD-L1 in early breast cancer. *ESMO Open*, 2(2):e000150, May 2017.
43. Vamsidhar Velcheti, Kurt A Schalper, Daniel E Carvajal, Valsamo K Anagnostou, Konstantinos N Syrigos, Mario Sznol, Roy S Herbst, Scott N Gettinger, Lieping Chen, and David L Rimm. Programmed death ligand-1 expression in non-small cell lung cancer. *Lab. Invest.*, 94(1):107–116, January 2014.
44. Joseph McLaughlin, Gang Han, Kurt A Schalper, Daniel Carvajal-Hausdorf, Vasiliki Pelekanou, Jamaal Rehman, Vamsidhar Velcheti, Roy Herbst, Patricia LoRusso, and David L Rimm. Quantitative assessment of the heterogeneity of PD-L1 expression in Non-Small-Cell lung cancer. *JAMA Oncol*, 2(1):46–54, January 2016.
45. Lilla Reiniger, Vanda Téglási, Orsolya Pipek, Livia Rójkó, Tibor Glasz, Áttila Vágvolgyi, Ilona Kovalszky, Márton Gyulai, Zoltán Lohinai, Erzsébet Rásó, József Timár, Balázs Dóme, Zoltán Szállási, and Judit Moldvay. Tumor necrosis correlates with PD-L1 and PD-1 expression in lung adenocarcinoma. *Acta Oncol.*, 58(8):1087–1094, August 2019.
46. Beth A Helmink, Sangeetha M Reddy, Jianjun Gao, Shaojun Zhang, Rafet Basar, Rohit Thakur, Kerem Yizhak, Moshe Sade-Feldman, Jorge Blando, Guangchun Han, Vancheswaran Gopalakrishnan, Yuanxin Xi, Hao Zhao, Rodabe N Amaria, Hussein A Tawbi, Alex P Cogdill, Wenbin Liu, Valerie S LeBleu, Fernanda G Kugeratski, Sapna Patel, Michael A Davies, Patrick Hwu, Jeffrey E Lee, Jeffrey E Gershenwald, Anthony Lucci, Reetakshi Arora, Scott Woodman, Emily Z Keung, Pierre-Olivier Gaudreau, Alexandre Reuben, Christine N Spencer, Elizabeth M Burton, Lauren E Haydu, Alexander J Lazar, Roberta Zapassodi, Courtney W Hudgens, Deborah A Ledesma, Sufey Ong, Michael Bailey, Sarah Warren, Disha Rao, Oscar Krijgsman, Elisa A Rozeman, Daniel Peeper, Christian U Blank, Ton N Schumacher, Lisa H Butterfield, Monika A Zelazowska, Kevin M McBride, Raghu Kalluri, James Allison, Florent Petitprez, Wolf Herman Fridman, Catherine Sautès-Fridman, Nir Hacohen, Katayoun Rezvani, Padmanee Sharma, Michael T Tetzlaff, Linghua Wang, and Jennifer A Wargo. B cells and tertiary lymphoid structures promote immunotherapy response. *Nature*, 577(7791):549–555, January 2020.
47. Rita Cabrita, Martin Lauss, Adriana Sanna, Marco Donia, Mathilde Skaarup Larsen, Shamik Mitra, Iva Johansson, Bengt Phung, Katja Harbst, Johan Vallon-Christersson, Alison van Schoick, Kristina Lövgren, Sarah Warren, Karin Jirstrom, Håkan Olsson, Kristian Pietras, Christian Ingvar, Karolin Isaksson, Dirk Schadendorf, Henrik Schmidt, Lars Bastholt, Ana Carneiro, Jennifer A Wargo, Inge Marie Svane, and Göran Jönsson. Tertiary lymphoid structures improve immunotherapy and survival in melanoma. *Nature*, 577(7791):561–565, January 2020.
48. Florent Petitprez, Aurélien de Reyniès, Emily Z Keung, Tom Wei-Wu Chen, Cheng-Ming Sun, Julien Calderaro, Yung-Ming Jeng, Li-Ping Hsiao, Laetitia Lacroix, Antoine Bougouin, Marco Moreira, Guillaume Lacroix, Ivo Nataro, Julien Adam, Carlo Lucchesi, Yec Han Laizet, Maud Toulmonde, Melissa A Burgess, Vanessa Bolejack, Denise Reinke, Khalid M Wani, Wei-Lien Wang, Alexander J Lazar, Christina L Roland, Jennifer A Wargo, Antoine Italiano, Catherine Sautès-Fridman, Hussein A Tawbi, and Wolf H Fridman. B cells are associated with survival and immunotherapy response in sarcoma. *Nature*, 577(7791):556–560, January 2020.
49. Ziqian Li, Jiawang Zhou, Junjie Zhang, Shiyang Li, Hongsheng Wang, and Jun Du. Cancer-associated fibroblasts promote PD-L1 expression in mice cancer cells via secreting CXCL5. *Int. J. Cancer*, 145(7):1946–1957, October 2019.
50. O Surova and B Zhivotovsky. Various modes of cell death induced by DNA damage. *Oncogene*, 32(33):3789–3797, August 2013.
51. Stephen P Jackson and Jiri Bartek. The DNA-damage response in human biology and disease. *Nature*, 461(7267):1071–1078, October 2009.
52. Arnaud J Legrand, Mattia Poletto, Daniela Pankova, Elena Clementi, John Moore, Francesco Castro-Giner, Anderson J Ryan, Eric O'Neill, Enni Markkanen, and Grigory L Dianov. Persistent DNA strand breaks induce a CAF-like phenotype in normal fibroblasts. *Oncotarget*, 9(17):13666–13681, March 2018.
53. Nicolas C Blessin, Ronald Simon, Martina Kluth, Kristine Fischer, Claudia Hube-Magg, Wenchao Li, Georgia Makrypidi-Fraune, Björn Wellge, Tim Mandelkow, Nicolaus F Debatin, Doris Höfelmayer, Maximilian Lennartz, Guido Sauter, Jakob R Izbicki, Sarah Miner, Franziska Büschel, Ria Uhlig, David Dum, Till Krech, Andreas M Luebke, Corinna Wittmer, Frank Jacobsen, Eike-Christian Burandt, Stefan Steurer, Waldemar Wilczak, and Andrea Hinsch. Patterns of TIGIT expression in lymphatic tissue, inflammation, and cancer. *Dis. Markers*, 2019:5160565, January 2019.
54. Mohamed Amgad, Elisabeth Specht Stovgaard, Eva Balslev, Jeppe Thagaard, Weijie Chen, Sarah Dudgeon, Ashish Sharma, Jennifer K Kerner, Carsten Denkert, Yinyun Yuan, Khalid AbdulJabbar, Stephan Wiener, Peter Savas, Leonie Voorwerk, Andrew H Beck, Anant Madabhushi, Johan Hartman, Manu M Sebastian, Hugo M Horlings, Jan Hudeček, Francesco Ciompi, David A Moore, Rajendra Singh, Elvire Roblin, Marcelo Luiz Balancin, Marie-Christine Mathieu, Jochen K Lennerz, Pawan Kirtani, I-Chun Chen, Jeremy P Braybrooke, Giancarlo Pruneri, Sandra Demaria, Sylvia Adams, Stuart J Schnitt, Sunil R Lakhani, Federico Rojo, Laura Comerma, Sunil S Badve, Mehrnosh Khojasteh, W Fraser Symmans, Christos Sotiropoulos, Paula Gonzalez-Ericsson, Katherine L Pogue-Geile, Rim S Kim, David L Rimm, Giuseppe Viale, Stephen M Hewitt, John M S Bartlett, Frédérique Penault-Llorca, Shom Goel, Huang-Chun Lien, Sibylle Loibl, Zuzana Kos, Sherene Loi, Matthew G Hanna, Stefan Michiels, Marleen Kok, Torsten O Nielsen, Alexander J Lazar, Zsuzsanna Bago-Horvath, Loes F S Kooreman, Jeroen A W M van der Laak, Joel Saltz, Brandon D Galas, Uday Kurkure, Michael Barnes, Roberto Salgado, Lee A D Cooper, and International Immuno-Oncology Biomarker Working Group. Report on computational assessment of tumor infiltrating lymphocytes from the international Immuno-Oncology biomarker working group. *NPJ Breast Cancer*, 6:16, May 2020.
55. Bruno Korbar, Andrea M Olofson, Allen P Mirafior, Catherine M Nicka, Matthew A Suriawinata, Lorenzo Torresani, Arief A Suriawinata, and Saeed Hassanpour. Deep learning for classification of colorectal polyps on whole-slide images. *J. Pathol. Inform.*, 8:30, July 2017.
56. Jonathan J Havel, Diego Chowell, and Timothy A Chan. The evolving landscape of biomarkers for checkpoint inhibitor immunotherapy. *Nat. Rev. Cancer*, 19(3):133–150, March 2019.
57. José Yélamos, Lucia Moreno-Lama, Jaime Jimeno, and Syed O Ali. Immunomodulatory roles of PARP-1 and PARP-2: Impact on PARP-Centered cancer therapies. *Cancers*, 12(2), February 2020.
58. Emma Beede, Elizabeth Baylor, Fred Hersch, Anna Iurchenko, Lauren Wilcox, Paisan Ruamviboonsuk, and Laura M Vardoulakis. A Human-Centered evaluation of a deep learning system deployed in clinics for the detection of diabetic retinopathy. In *Proceedings of the 2020 CHI Conference on Human Factors in Computing Systems*, CHI '20, pages 1–12, New York, NY, USA, April 2020. Association for Computing Machinery.
59. Pegah Khosravi, Ehsan Kazemi, Marcin Imielinski, Olivier Elemento, and Iman Hajira-souliha. Deep convolutional neural networks enable discrimination of heterogeneous digital pathology images. *EBioMedicine*, 27:317–328, January 2018.
60. Halla Mohamed Ragab, Nervana Samy, Mie Afify, Nabila Abd El Maksoud, and Hebatallah Mohamed Shaaban. Assessment of ki-67 as a potential biomarker in patients with breast cancer. *J. Genet. Eng. Biotechnol.*, 16(2):479–484, December 2018.
61. Shivam Kalra, H R Tizhoosh, Sultaan Shah, Charles Choi, Savvas Damaskinos, Amir Safarpour, Sobhan Shafiei, Morteza Babaie, Phedias Diamandis, Clinton J V Campbell, and Liron Pantanowitz. Pan-cancer diagnostic consensus through searching archival histopathology images using artificial intelligence. *NPJ Digit Med*, 3:31, March 2020.
62. Hassan M Rostam, Paul M Reynolds, Morgan R Alexander, Nikolaj Gadegaard, and Amir M Ghaemmaghami. Image based machine learning for identification of macrophage subsets. *Sci. Rep.*, 7(1):3521, June 2017.
63. Evita T Sadimin and David J Foran. Pathology imaging informatics for clinical practice and investigative and translational research. *N. Am. J. Med. Sci.*, 5(2):103–109, April 2012.
64. Tian Zhang, Raghu Ramakrishnan, and Miron Livny. BIRCH: an efficient data clustering method for very large databases. *SIGMOD Rec.*, 25(2):103–114, June 1996.
65. Andrew Rosenberg and Julia Hirschberg. V-measure: A conditional entropy-based external cluster evaluation measure. In *Proceedings of the 2007 joint conference on empirical methods in natural language processing and computational natural language learning (EMNLP-CoNLL)*, pages 410–420, 2007.
66. Michael W Dority, Lauren M Saunders, Christine Queitsch, Stanley Fields, and Cole Trapnell. Dimensionality reduction by UMAP to visualize physical and genetic interactions. *Nat. Commun.*, 11(1):1537, March 2020.
67. Vésteinn Thorsson, David L Gibbs, Scott D Brown, Denise Wolf, Dante S Bortone, Tai-Hsien Ou Yang, Eduard Porta-Pardo, Galen F Gao, Christopher L Plaisier, James A Eddy, Elad Ziv, Aedin C Culhane, Evan O Paul, I K Ashok Sivakumar, Andrew J Gentles, Ranaq Malhotra, Farshad Farshidfar, Antonio Colaprico, Joel S Parker, Lisle E Mose, Nam Sy Vo, Jianfang Liu, Yuxin Liu, Janet Rader, Varsha Dhankani, Sheila M Reynolds, Reanne Bowby, Andrea Califano, Andrew D Cherniack, Dimitris Anastassiou, Davide Bedognetti, Younes Mokrab, Aaron M Newman, Arvind Rao, Ken Chen, Alexander Krasnitz, Hai Hu, Thathiane M Malta, Houtan Noshahr, Chandra Sekhar Pedamallu, Susan Bullman, Akinyemi I Ojesina, Andrew Lamb, Wanding Zhou, Hui Shen, Toni K Choueiri, John N Weinstein, Justin Guinney, Joel Saltz, Robert A Holt, Charles S Rabkin, Cancer Genome Atlas Research Network, Alexander J Lazar, Jonathan S Serody, Elizabeth G Demicco, Mary L Disis, Benjamin G Vincent, and Ilya Shmulevich. The immune landscape of cancer. *Immunity*, 48(4):812–830.e14, April 2018.
68. Yoav Benjamini and Yosef Hochberg. Controlling the false discovery rate: A practical and powerful approach to multiple testing. *J. R. Stat. Soc. Series B Stat. Methodol.*, 57(1):289–300, 1995.
69. Cancer Genome Atlas Research Network, John N Weinstein, Eric A Collisson, Gordon B Mills, Kenna R Mills Shaw, Brad A Ozenberger, Kyle Ellrott, Ilya Shmulevich, Chris Sander, and Joshua M Stuart. The cancer genome atlas Pan-Cancer analysis project. *Nat. Genet.*, 45(10):1113–1120, October 2013.
70. Theo A Knijnenburg, Linghua Wang, Michael T Zimmermann, Nyasha Chambwe, Galen F Gao, Andrew D Cherniack, Huihui Fan, Hui Shen, Gregory P Way, Casey S Greene, Yuxin Liu, Rehan Akbani, Bin Feng, Lawrence A Donehower, Chase Miller, Yang Shen, Mostafa Karimi, Haoran Chen, Pora Kim, Peilin Jia, Eve Shinbrot, Shaojun Zhang, Jianfang Liu, Hai Hu, Matthew H Bailey, Christina Yau, Denise Wolf, Zhongming Zhao, John N Weinstein, Lei Li, Li Ding, Gordon B Mills, Peter W Laird, David A Wheeler, Ilya Shmulevich, Cancer Genome Atlas Research Network, Raymond J Monnat, Jr, Yonghong Xiao, and Chen Wang. Genomic and molecular landscape of DNA damage repair deficiency across the cancer genome atlas. *Cell Rep.*, 23(1):239–254.e6, April 2018.
71. Noah Simon, Jerome Friedman, Trevor Hastie, and Robert Tibshirani. A Sparse-Group lasso. *J. Comput. Graph. Stat.*, 22(2):231–245, April 2013.

Methods

Dense, high-resolution prediction of cell and tissue types using convolutional neural networks. In order to compute histopathological image features for each slide, it was necessary to first generate cell and tissue predictions per WSI. To this end, we asked a network of board-certified pathologists to label WSIs with both polygonal region annotations based on tissue type (cancer tissue, cancer-associated stroma, necrotic tissue, and normal tissue or background) and point annotations based on cell type (cancer cells, lymphocytes, macrophages, plasma cells, fibroblasts, and other cells or background). This collection of expert annotations was then used to train six-class cell type and four-class tissue-type classifiers.

Several steps were taken to ensure the accuracy and generalizability of our models. First, it was important to recognize that common cell and tissue types, such as cancer-associated stroma or cancer cells, show morphological differences between BRCA, LUAD, LUSC, SKCM, and STAD. As a result, we trained separate cell- and tissue-type detection models for each of these five cancer types, for a total of ten models. Second, it was important to ensure that our models did not overfit to the histological patterns found in the training set. To avoid this, we followed the conventional protocol of splitting our data into training, validation, and test sets, and incorporated additional annotations of the same five cancer types from PathAI's databases into the model development process. Together, these datasets represented a wide diversity of examples for each class in each cancer type, thus improving the generalizability of these models beyond the TCGA dataset.

Using the combined dataset of annotated TCGA and additional WSIs, we trained deep convolutional neural networks (CNN) to output dense pixelwise cell- and tissue-type predictions at a subcellular spatial resolution of two and four microns, respectively (spatial resolution dictated by stride). To ensure that our models achieved sufficient accuracy for feature extraction, models were trained in an iterative process, with each updated model's predictions visualized as heatmaps to be reviewed by board-certified pathologists. In heatmap visualizations, tissue categories were segmented into colored regions, while cell types were identified as colored squares. This process continued until there were minimal systematic errors and the pathologists deemed the model sufficiently trustworthy for feature extraction.

Pathologist validation of cell- and tissue-type predictions. During the CNN training process, we worked iteratively with three board-certified pathologists to conduct subjective evaluation of model predictions to inform multiple rounds of training. CNN models were initially trained on a set of primary annotations collected from the pathologist network. Following the conclusion of each training round (defined by model convergence), predicted cell and tissue heatmaps were reviewed for systematic errors (e.g. overprediction of fibroblasts, macrophages, and plasma cells, underprediction of necrotic tissue). New annotations would then

be collected from the pathologist network focusing on areas of improvement (e.g. mislabeled macrophages) to initiate a subsequent training round.

Tissue-based feature extraction. Using the tissue-type predictions, we extracted 163 different region-based features from each WSI in the TCGA dataset. Each of these features belonged to one of three general categories.

The first category consisted of areas ($n = 13$ HIFs). By simple pixel summation, we computed the total areas (in mm^2) of cancer tissue, cancer-associated stroma, cancer tissue plus cancer-associated stroma, regions at the cancer-stroma interface, and necrosis in each slide. These features are interpretable and technically attainable by human pathologists, but would be prohibitively time-consuming and inconsistent across pathologists to calculate in practice.

The second category, which contributed the bulk of the features, made use of the publicly available `scikit-image.measure.regionprops` module to find the connected components of each of these tissue types at the pixel-level using eight-connectivity. Once these connected components were found, we used both library-provided and self-implemented methods to extract a series of morphological features ($n = 125$ HIFs), similar to the approach suggested by Wang et al. in 2018²³. These HIFs measured a wide variety of tissue characteristics, ranging from quantitative, size-based measures like the number of connected components, major and minor axis lengths, convex areas, and filled areas, to more qualitative, shape-based measures like Euler numbers, lacunarity, and eccentricity. Recognizing the log-distribution of connected component size, we computed these features not just across all connected components, but also for both the largest connected component only and across the most "significant" connected components, defined as components larger than 10% the size of the largest connected component. In aggregating metrics across considered components, we incorporated both averages and standard deviations of HIFs (e.g. standard deviation of eccentricities of significant regions of necrosis), to capture both summary metrics and metrics of intratumor heterogeneity.

The third category of features captures tissue architecture ($n = 25$ HIFs). Inspired by Lennon et al.²⁴, we calculated the fractal dimensions and solidity measures of different tissue types, capturing both the roundness and filled-ness of the tissue, under the hypothesis that the ability for these measures to separate different subtypes of lung cancer might translate to a similar ability to predict clinically-relevant phenotypes. These features allowed us to capture information about how tissue filled up space, rather than just the summative sizes and shapes captured by the first and second categories.

Cell- and tissue-based feature extraction. After obtaining six-class cell-type predictions for each pixel of a WSI, we generated five binary masks corresponding to each of the five specified cell types. We then combined cell- and tissue-level masks to compute properties of each cell type in each tissue type (e.g. fibroblasts in cancer-associated stroma), extracting 444 HIFs.

An initial group of features that were readily calculable from our model predictions included simple counts and densities of cell types in different tissue types. For example, an overlay of a particular slide's lymphocyte detection mask on top of the same slide's cancer-associated stroma mask could be used to calculate the number of TILs on a given slide. We could then divide this number by the area of cancer-associated stroma to find the associated density of TILs on the slide. By taking the "outer product" of cell and tissue types, we derived a wide array of composite features. In particular, we calculated counts, proportions, and densities of cells across different tissue types (e.g. density of macrophages in cancer-associated stroma versus in cancer tissue), under the hypothesis that these measures capture information that raw counts could not. To capture information regarding cell-cell proximity and interactions, we also calculated counts and proportions of each cell type within an 80 micron radius of each other cell type (e.g. count of lymphocytes within an 80 micron radius of fibroblasts). Cell-level counts, densities, and proportions comprised 264 HIFs.

For each cell-tissue combination, we next applied the Birch clustering method (as implemented in the `sklearn.cluster` Python module) to partition cells into clusters⁶⁴. To fit clustering structures as closely as possible to the spatial relationships found between cell types on the slide, we set a threshold of 100, a branching factor of 10, and allowed the algorithm to optimize the number of clusters returned. We used the returned clusters to calculate a series of features designed to capture spatial relationships between individual cells types within a given tissue type, including number of clusters, cluster size mean and standard deviation (SD), within-cluster dispersion mean and SD, cluster extent mean and SD, the Ball-Hall Index, and Calinski-Harabasz Index ($n = 180$ HIFs). For metrics where cluster exemplars were needed, the subcluster centers returned by the Birch algorithm were used.

Patient-level aggregation. Patients with multiple tissue samples were represented by the single sample with the largest area of cancer tissue plus cancer-associated stroma, computed during tissue-based feature extraction. All subsequent analyses were conducted at the patient level.

HIF clustering. Due to underlying biological relationships as well as the HIF generation process, there is significant correlation structure between many of the features. This presents a challenge of feature selection as much of the information contained in one feature will also be present in another. It also makes it difficult to control for multiple hypothesis testing, because the underlying number of tested hypotheses is significantly fewer than the number of features computed.

To identify groups of correlated HIFs, we clustered features via hierarchical agglomerative clustering using complete linkage, a cluster cutoff of 0.95, and pairwise correlation distance ($1 - \text{absolute Spearman correlation}$) as the distance metric. We defined a set of HIF clusters for each cancer type independently, as well as another set for pan-cancer analyses (Supplemental Data 1). Clustering correlated features allows us to summarize the true underlying number of

tested hypotheses.

Visualization of cancer types in HIF space. Uniform Manifold Approximation and Projection (UMAP) was applied for dimensionality reduction and visualization of patient samples from the 607-dimension HIF space into two dimensions (using parameters: number of neighbors = 15, training epochs = 500, distance metric = euclidean). The V-Measure was computed to compare BRCA, STAD, SKCM, and NSCLC (LUAD and LUSC combined) classes against clusters generated by k-means ($k = 4$) applied to the 2-D UMAP projection^{65,66}. To quantify differences between cancer types, HIF values were normalized pan-cancer into Z-scores. Median Z-scores were then computed per cancer type across twenty HIFs, each representing one of twenty HIF clusters defined pan-cancer. Representative HIFs were selected based on subjective interpretability and high variance across cancer types. To determine the statistical significance of median Z-scores that were greater in one cancer type relative to others, P-values were estimated with the one-sided Mann-Whitney U-test, considering NSCLC subtypes LUAD and LUSC as one type.

Validation of HIFs against molecular markers. To validate the ability of HIFs to capture meaningful cell- and tissue-level information, we computed Spearman correlations between HIFs and four canonical immune markers from the PanImmune dataset⁶⁷: (1) leukocyte infiltration, (2) IgG expression, (3) TGF- β expression, and (4) wound healing. Immune markers were quantified by mapping mRNA sequencing reads against gene sets associated with known immune expression signatures. To estimate the correlation between HIF clusters and immune markers, we computed the median absolute Spearman correlation per cluster and combined dependent P-values associated with individual correlations via the Empirical Brown's method³⁵. To control the false discovery rate, combined P-values per cluster were then corrected using the Benjamini-Hochberg procedure⁶⁸. Correlation analyses were conducted for cancer types collectively and individually, using HIF clusters defined across all cancer types for assessment of concordance.

In addition, image-based cell quantifications for leukocyte fraction, lymphocyte fraction, and plasma cell fraction were validated by Spearman correlation to their sequencing-based equivalents from matched TCGA tumor samples, computed using CIBERSORT⁶⁷. CIBERSORT (cell-type identification by estimating relative subsets of RNA transcripts) uses an immune signature matrix for deconvolution of observed RNA-Seq read counts into estimates of relative contributions between 22 immune cell profiles³⁴.

Molecular phenotype label curation. PD-1, PD-L1, and CTLA-4 expression data for each cancer type were collected from the PanImmune dataset⁶⁷, while TIGIT expression data was collected from the National Cancer Institute Genomic Data Commons⁶⁹. PD-1, PD-L1, CTLA-4, and TIGIT expression levels were quantified from mapped mRNA reads

against genes PDCD1, CD274, CTLA-4, and TIGIT, respectively, and normalized as Z-scores across all cancer types in TCGA. Homologous recombination deficiency (HRD) scores were collected from Knijnenburg et al.⁷⁰. The HRD score was calculated as the sum of three components: 1) number of sub-chromosomal regions with allelic imbalance extending to the telomere, 2) number of chromosomal breaks between adjacent regions of least 10 Mb (mega base pairs), and 3) number of loss of heterozygosity regions of intermediate size (at least 15 Mb but less than whole chromosome length). Continuous immune checkpoint protein expression and HRD scores were binarized to high versus low classes using gaussian mixture model (GMM) clustering with unequal variance (Supplemental Figure 3). The binary threshold was defined as the intersection of the empirical densities between the two GMM-defined clusters. To evaluate the extent to which prediction tasks were correlated, Pearson correlation and percentage agreement metrics were computed pan-cancer ($n = 1,893$ patients) between the five molecular phenotypes in continuous and binarized form, respectively (Supplemental Figure 6).

Hold-out set definition by TCGA tissue source site.

TCGA provides tissue source site information, which denotes the medical institution or company that provided the patient sample. For each prediction task (described below), a hold-out set was defined as approximately 20-30% of patient samples obtained from sites not seen in the training set (Supplemental Table 4). This validation methodology enables us to demonstrate model generalizability across varying patient demographics and tissue collection processes intrinsic to different tissue source sites. Patient barcodes corresponding to hold-out and training sets are provided in Supplemental Data 2.

Supervised prediction of molecule phenotypes.

We conducted supervised prediction of binarized high versus low expression of five clinically-relevant phenotypes: (1) PD-1 expression, (2) PD-L1 expression, (3) CTLA-4 expression, (4) HRD score, and (5) TIGIT expression. Predictions were conducted pan-cancer as well as for cancer types individually. SKCM was excluded from prediction tasks 1-4 due to insufficient outcome labels (number of observations < 100 for tasks 1-3; number of positive labels < 10 for task 4). For each prediction task, we trained a logistic sparse group lasso (SGL) model⁷¹ tuned by nested cross validation (CV) with three outer folds and five inner folds using the corresponding training set. SGL provides regularization at both an individual covariate (as in traditional lasso) and user-defined group level, thus encouraging group-wise and within group sparsity. The HIF clusters defined per cancer type and pan-cancer (previously described) were inputted as groups. HIFs were normalized to mean = 0 and SD = 1. In accordance with nested CV, hyper-parameter tuning was conducted using the inner loops and mean generalization error and variance were estimated from the outer loops. The three tuned models, each trained on two of the three outer folds and evaluated on the third outer fold, were ensembled by averaging predicted probabilities for final evaluation (reported in Fig-

ure 6a; Supplemental Table 5) on the hold-out set. Hold-out performance was evaluated by AUROC and AUPRC. To identify predictive features, beta values from the three outer fold models were averaged to obtain ensemble beta values per HIF (see Figure 6b caption for more details).

Statistical analysis. To compute 95% confidence intervals for each prediction task, we generated empirical distributions of AUROC and AUPRC metrics each consisting of 1000 bootstrapped metrics. Bootstrapped metrics were obtained by sampling with replacement from matched model predictions (probabilities) and true labels for the corresponding hold-out set, and re-computing AUROC and AUPRC on these two bootstrapped vectors. P-values for ensemble beta values of predictive HIFs were computed using a permutation test with 1000 iterations. During each iteration, labels in the training set were permuted and the previously described training process of nested CV and ensembling was re-applied to generate a new set of ensemble beta values per HIF. P-values for individual HIFs were then obtained by comparing beta values in the original ensemble model against the corresponding null distribution of ensemble beta values. Individual HIF P-values were combined into cluster-level P-values via the Empirical Brown's method³⁵ and corrected using the Benjamini-Hochberg procedure⁶⁸.

Data availability. The Cancer Genome Atlas dataset may be accessed at <https://www.cancer.gov/about-nci/organization/ccg/research/structural-genomics/tcga>. The relevant data consists of 2,917 hematoxylin and eosin-stained WSIs of breast cancer, non-small cell lung adenocarcinoma, non-small cell lung squamous cell carcinoma, gastric adenocarcinoma, and skin cutaneous melanoma specimens from 2,634 patients.

Code availability. The source code used to generate figures in this work can be downloaded from: <https://github.com/jamesdiao/hif2gene>.